*Clays and Clay Minerals*, Vol. 69, No. 4:425–433, 2021

# LAYERED DOUBLE HYDROXIDE-BASED MRI/CT DUAL MODAL CONTRASTING AGENT WITH HOMOGENEOUS PARTICLE SIZE

Sang-Yong Jung[1], Jin Kuen Park[2]*, and Jae-Min Oh[1]*

[1]Department of Energy and Materials Engineering, Dongguk University-Seoul, Seoul 04620, Republic of Korea
[2]Department of Chemistry, Hankuk University of Foreign Studies, Yongin 17035, Republic of Korea

**Abstract**—The development of nanoparticles incorporating $Gd^{3+}$ has attracted interest in the field of contrasting nanomedicine for magnetic resonance (MR) and computed tomography (CT). In order to achieve an effective contrasting performance, the amount and stability of Gd incorporated as well as particle-size control of the nanoparticles should be considered simultaneously. In the current study, Gd-diethylenetriaminepentaacetate(Gd-DTPA) was incorporated into layered double hydroxide (LDH) to meet the physicochemical properties required for MR-CT dual contrasting nanomedicine. Strategically, the particle size and nanometer incorporation of Gd-DTPA into LDH (GL-R hybrid) were controlled homogeneously using the reverse micelle method. X-ray diffraction showed that the hybrid obtained possessed a hydrotalcite phase. Dynamic light scattering and electron microscopic analyses showed that the hybrid had a controlled size of <200 nm with significant homogeneity. Fast Fourier-transform of transmission electron microscopy confirmed that the platelets of the GL-R hybrids were oriented randomly to form inter-particle space, enabling the Gd-DTPA moiety to be encapsulated stably. The encapsulation efficiency of Gd-DTPA was 20.8%, which was sufficiently high compared with other Gd-DTPA-incorporatedLDH. According to X-ray photoelectron spectroscopy and Fourier-transform infrared spectroscopy, Gd-DTPA incorporated in the hybrid preserved its structure intact. Its potential as a dual modal contrast agent was demonstrated by measuring the concentration-dependent Hounsfield unit and magnetic resonance relaxivity, which were determined to be 230 at 2 mg/mL and 5.8 in the range ~0.2–1 mM-Gd, respectively.

**Keywords**—Contrast agent · Dual modal · Gd-DTPA · Layered double hydroxide · Reverse micelle method · Size control

## INTRODUCTION

Imaging-based diagnostic technologies such as magnetic resonance imaging (MRI), computed tomography (CT), positron emission tomography (PET), and single-positron emission computed tomography (SPECT) are utilized widely in clinical medicine (Wattjes et al., 2015; Meng et al., 2019; Ma & Liu, 2020; Zhang et al., 2020). In order to obtain images with high resolution and accuracy in diagnosis, contrast agents (CA) are administered to patients. For example, iodinated contrast agents are utilized widely in CT imaging, especially to investigate dysfunction of the thyroid gland (Lusic & Grinstaff, 2013); radionuclide F-18-tagged glucose is administered to diagnose various types of tumors at a systemic level, utilizing PET instruments (Alauddin, 2012).

Recent advances in nanotechnology have improved the efficacy of CA and also addressed the disadvantages of molecular CA such as rapid clearance, unspecific systemic distribution, toxicity, etc. (Aime & Caravan, 2009; Vithanarachchi & Allen, 2012; Li et al., 2013a, 2013b). Various nanoplatforms are under development commercially and academically. Liposomal CT contrast agent is a well known example of commercialized nanotechnology based on CA in which iodinated phosphatidylcholine forms a liposomal bilayer with high iodine loading. Iron oxide nanoparticles are not just commercialized as an MRI contrasting agent but also studied academically in order to reinforce the functionalities (Li et al., 2013a). Due to the biocompatibility, significant X-ray attenuation ability, and easy surface modification, noble metals such as Au and Pt in nanoparticle form are attracting research interest for CT nanodiagnostics (Seltzer et al., 1984; Pedrosa & Baptista, 2015; Xu et al., 2019).

Among various nanoplatforms, layered double hydroxide (LDH) has been highlighted due to its unique properties for biomedical application. The LDH is one of the family of layered materials, consisting of positively charged metal hydroxide layers and interlayer anions. The general chemical formula of LDH is represented as $[M^{2+}_{1-x}M^{3+}_{x}(OH)_2]^{x+}(A^{n-}_{x/n})\cdot yH_2O$, where $M^{2+}$ and $M^{3+}$ represent divalent and trivalent cations to form the layer component and $A^{n-}$ is an interlayer anion. LDH can accommodate safely various chemical species in the interlayer space (Choy, 2004; Choy et al., 2008; Kim et al., 2012, 2013) and its solubility in weak acidic conditions can enable bioresorbability (Kriven et al., 2004) and biocompatibility (Choi et al., 2010). Furthermore, size-controlled LDH exhibited high cellular uptake efficiency to cancer cells (Oh et al., 2006b, 2009) and tumor targeting ability at the systemic level (Choi et al., 2010). In this regard, extensive research has indicated the great potential of LDH as a drug or gene delivery carrier (Choy et al., 2000, 2004; Kim et al., 2014). As the drug-delivery concept could be applied to contrasting agents, LDH is considered an alternative candidate for use as a CA nanoplatform.

* E-mail address of corresponding author: jinkpark@hufs.ac.kr
DOI: 10.1007/s42860-021-00142-9

© The Clay Minerals Society 2021

The paper is based on a presentation made during the 4th Asian Clay Conference, Thailand, June 2020.

https://doi.org/10.1007/s42860-021-00142-9 Published online by Cambridge University Press

Several scientific studies have dealt with nanodiagnostic applications of LDH such as manganese-based LDH for MRI (Li et al., 2017; Xie et al., 2019), radioisotope-incorporated LDH for PET or SPECT (Musumeci et al., 2010; Kim et al., 2016), and Gd-DTPA intercalated LDH for MRI, etc. (Xu et al., 2007; Kim et al., 2008). Those pioneering studies suggested innovative ways not only to improve the performance of CA but also to provide CA with various functionalities. For the practical application of LDH-based nanodiagnostics, the next steps should focus on the following two points. (1) Nanodiagnostic CA with a small particle size and with narrow distribution in terms of biocompatibility and long-term circulation are required. Due to their anisotropic properties, LDH particles tend to agglomerate through strong edge-to-face interaction (Gursky et al., 2006), hindering the preparation of small and homogeneous particle sizes in the hydrodynamic phase. (2) An alternative synthesis strategy to accommodate the contrasting moiety is necessary as previous approaches did not consider economic points such as the yield and loss of reactants.

In order to solve the above-mentioned challenges, a modified reverse-micelle method was adopted (Hu et al., 2007). The method is considered to facilitate crystal growth of the LDH and incorporation of the contrasting moiety simultaneously in the confined space of the micelle. The particle growth and the degree of aggregation would be restricted, giving rise to a homogeneous reaction among precursors. In the current contribution, Gd-DTPA, an excellent molecule as an MRI-contrasting agent (Kim et al., 2008) as well as a CT-contrasting agent (Bloem & Wondergem, 1989), was incorporated into LDH through a reverse micelle method to obtain an homogeneous and effective dual contrasting agent. The present authors hypothesized that the hybridization between Gd-DTPA and LDH would result in a particle with a concentrated Gd-DTPA moiety; in addition, the reverse-micelle method would prohibit unexpected growth of particles to enhance homogeneity of contrasting power. In order to control the hierarchical structure of hybrids, both coprecipitation and reconstruction method were applied respectively to prepared hybrids between Gd-DTPA and LDH. The influence of hierarchical structure and particle homogeneity of hybrids on dual contrasting power will be demonstrated below.

## EXPERIMENTAL

### *Materials*

Aluminum nitrate nonahydrate ($Al(NO_3)_3{\cdot}9H_2O$), hexadecyltrimethylammonium bromide ($CH_3(CH_2)_{15}N(Br)(CH_3)_3$, CTAB), and diethylenetriaminepentaacetic acid gadolinium(III) dihydrogen salt hydrate ($C14H_{20}GdN_3O_{10}{\cdot}xH_2O$, Gd-DTPA) were purchased from Sigma-Aldrich, Inc. (St. Louis, Missouri, USA). Magnesium nitrate hexahydrate ($Mg(NO_3)_2{\cdot}6H_2O$) was purchased from Junsei Chemical Co., Ltd. (Tokyo, Japan). Sodium hydroxide (NaOH), sodium bicarbonate ($NaHCO_3$), and ethyl alcohol ($C_2H_5OH$, absolute grade) were obtained from Daejung Chemicals and Metal Co., Ltd. (Siheung, Korea). Acetone ($C_3H_6O$, extra pure grade) and 1-butanol ($C_4H_{10}O$, extra pure grade) were obtained from Samchun Pure Chemical Co., Ltd. (Seoul, Korea). Cyclohexane ($C_6H_{12}$, extra pure grade) was purchased from Duksan Company (Seoul, Korea).

### *Preparation of Gd-incorporated LDHs, GL-R, and GL-C*

In order to prepare Gd-incorporated LDH hybrid with an homogeneous particle size (GL-R), the reverse micelle method was utilized referring to previous reports (Zhang et al., 2001; Hu et al., 2007). A microemulsion was prepared by adding 5 g of CTAB and 7.4 mL of 1-butanol to cyclohexane (200 mL). Three kinds of reaction solution – 2.07 mL of mixed metal solution (2.4 mol/L $Mg^{2+}$ and 0.8 mol/L $Al^{3+}$), 5 mL of Gd-DTPA solution (~0.48~0.5 mol/L), 3 mL of sodium hydroxide solution (0.02 mol/L) – were added successively to the microemulsion.

After stirring for 24 h at room temperature, the suspension was centrifuged and the surfactant was removed by the following process. First, the precipitate was redispersed in water:ethanol (1:1) at 75°C for 8 h. The precipitate was again collected by centrifugation and redispersed in acetone at 50°C for 8 h. Finally the precipitate obtained was dried at room temperature for 8 h.

For comparative study, GL without reverse micelle treatment was prepared by conventional coprecipitation (GL-C). With the same stoichiometry, three solutions – 2.07 mL of mixed metal solution (2.4 mol/L $Mg(NO_3)_2{\cdot}6H_2O$ and 0.8 mol/L $Al(NO_3)_3{\cdot}9H_2O$), 5 mL of Gd-DTPA solution (~0.48~0.5 mol/L), 3 mL of sodium hydroxide solution (0.02 mol/L) – were mixed and stirred for 24 h under ambient conditions. The stoichiometry and concentration of reactants in the GL-C synthesis were controlled in the same way as those in the GL-R synthesis. Then, the precipitate was washed and dried as for GL-R.

### *Characterization*

Powder X-ray diffraction (XRD) patterns (Bruker D2 PHASER, Billerica, Massachusetts, USA), using Ni-filtered CuK$\alpha$ radiation ($\lambda$ = 1.5418 Å) with step sizes and time/step of 0.02°2$\theta$ and 0.2 s, respectively, were obtained to investigate the crystallite size and crystal structure of GL-R and GL-C. The particle morphology and distribution of GL-R and GL-C were observed by field emission scanning electron microscopy (FE-SEM, JEOL 7100F, Tokyo, Japan). For SEM measurements, 0.5 mg/mL of suspension prepared with GL-R and GL-C in ethanol was dispersed by tapping the suspension gently. Then the suspension was placed dropwise onto a Si wafer. High-resolution transmission electron microscopy (HR-TEM) and fast Fourier transform (FFT) using a Titan G2 ChemiSTEM Cs Probe of FEI company (Hillsboro, Oregon, USA) were used at an accelerating voltage of 200 kV. For TEM measurements, sample suspensions were placed on a Tedpella, Inc. (Redding, California, USA) 200 mesh Cu grid. The hydrodynamic radius was measured with an Otsuka electronics ELSZ-1000 (Osaka, Japan) instrument at a suspension concentration of 0.1 mg/mL. The accumulation and repetition times were 50 s and 3 s, respectively. Fourier-transform infrared (FTIR)

https://doi.org/10.1007/s42860-021-00142-9 Published online by Cambridge University Press

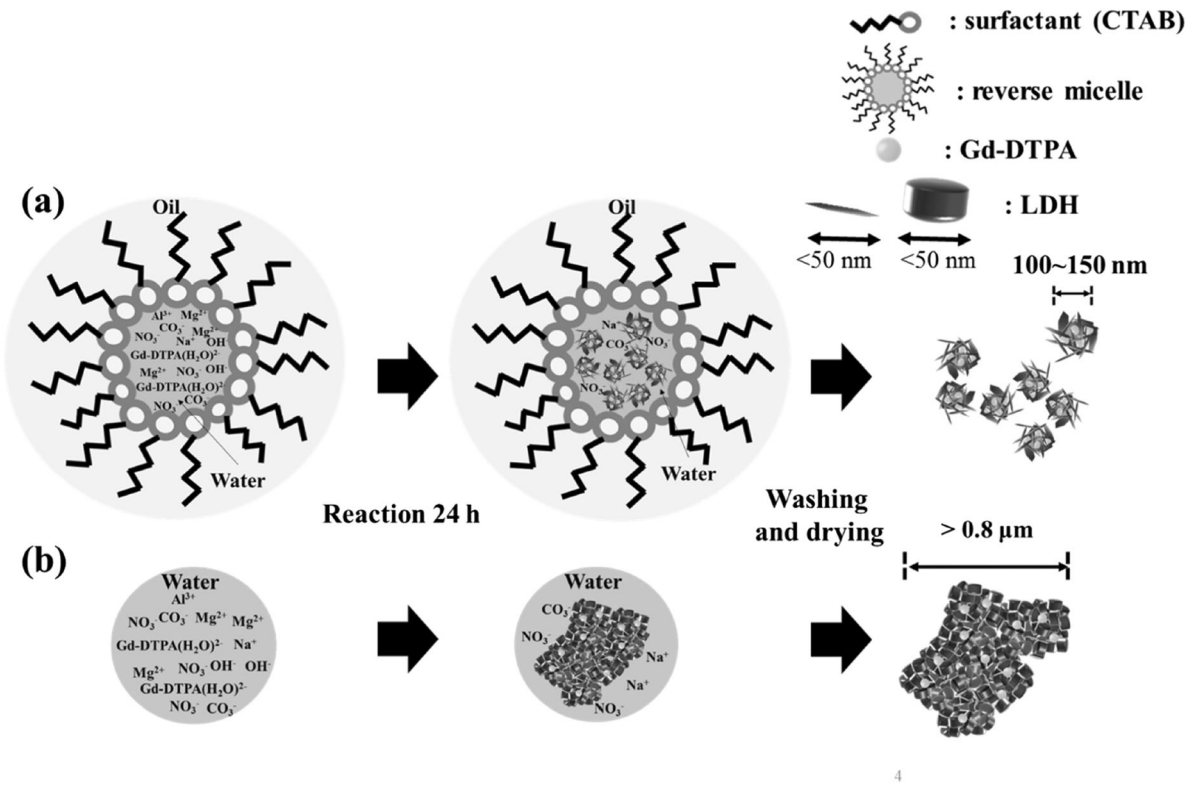



**Fig. 1** Schematic illustration of the synthesis strategy

attenuated total reflectance (ATR) spectroscopy (Perkin Elmer Spectrum 65, Perkin Elmer Co. Ltd., Waltham, Massachusetts, USA) was done in the powder state. X-ray photoelectron spectroscopy (XPS) was carried out using a Thermo K alpha+ instrument (Waltham, Massachusetts, USA) operating at a pressure of $<5 \times 10^{-8}$ mbar. AlKα radiation (1486.7 eV) at 50 eV pass energy (the energy with which all photoelectrons will enter the spectrometer) was applied and the scan resolution was 0.1 eV.

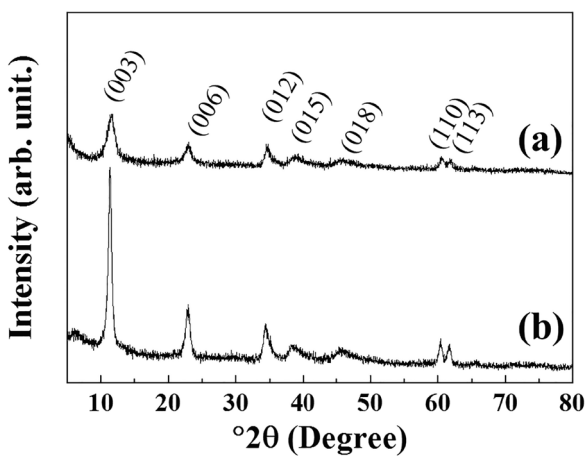



**Fig. 2** XRD patterns of **a** GL-R and **b** GL-C

*CT/MRI Test*

To investigate the concentration-dependent Hounsfield unit (HU), a GL-R stock suspension was prepared in deionized water (2 mg/mL) and then diluted to 1, 0.8, 0.4, and 0.2 mg/mL. Then 200 μL of each diluted suspension and the stock suspension was put into each well of a 96 well plate after vortexing for 2 min. CT measurement was carried out with a Biograph mCT (Siemens Medical Solutions Inc., Munich, Germany) instrument operating at 120 kV, 35 mA, and with a 17.55 s scan time.

In order to assess the MRI contrasting efficiency of GL-R, a sample was dispersed in pH 7 phosphate-buffered saline to prepare a stock suspension with 1 mmol/L of $Gd^{3+}$ ion concentration, which was then diluted to 0.8, 0.6, 0.4, and 0.2 mM. The longitudinal relaxation ($T_1$) time was measured at 1, 0.8, 0.6, 0.4, and 0.2 mmol/L with a Bruker 4.7 T MRI (Billerica, Massachusetts, USA), equipped with a 72 mm solenoid coil. MR images were acquired with flipped angle of 90°, TR/TE/NEX 100/7.8/1, FOV = 5.4 cm × 7.4 cm, data matrix 128 × 128, slice thickness 1 mm.

## RESULTS AND DISCUSSION

The Gd-complex-incorporated LDH with sufficient Gd content, small particle size, and homogeneous distribution (GL-R) was obtained by the reverse-micelle method (Fig. 1a). Although the coprecipitation method is well known and the easiest way to synthesize LDH, it has limitations in terms of size control and

https://doi.org/10.1007/s42860-021-00142-9 Published online by Cambridge University Press

**Table 1** Lattice parameters and crystallite size for GL-R and GL-C

| | Lattice parameter (Å) | | Crystallite size (nm) (*hkl*) | |
|---|---|---|---|---|
| | *a* | *c* | (110) | (003) |
| GL-R | 3.05 | 23.83 | 10.43 | 5.70 |
| GL-C | 3.06 | 23.32 | 12.93 | 14.46 |

particle aggregation (Fig. 1b). The LDHs prepared by simple coprecipitation tend to agglomerate through strong edge-to-face interaction which is generally found in anisotropic clay materials (Gursky et al., 2006). Taking into account the medical application of LDH through vascular injection, large agglomerates may cause problems such as lethal clogging in blood vessels. Furthermore, to incorporate a Gd-moiety in the hybrid easily, another strategy was needed. Generally, guest molecules are intercalated between LDH layers for stabilization and functionalization. A neatly intercalated phase is often difficult to obtain and the process requires a large amount of guest in order to achieve a concentration gradient. In the reverse-micelle method, the small LDH crystallites and Gd-DTPA molecules would be hybridized homogeneously through charge–charge interaction (positive layer charge of LDH-negative charge of DTPA ligand). As Gd-DTPA is well known as a $T_1$-MRI contrast agent and has an X-ray attenuating property suitable for a CT contrast agent, homogeneous GL-R prepared thus is considered to have multimodal contrasting ability.

The crystal structure of GL-C and GL-R was analyzed using XRD (Fig. 2). Diffraction peaks of GL-R were observed at 11.62, 23.14, 34.74, 39.23, 45.98, 60.61, and 61.84°2θ, corresponding to the crystal planes (003), (006), (012), (015), (018), (110), and (113), respectively, of hydrotalcite (JCPDS No.14-0191). Similarly, the XRD pattern of GL-C showed peaks at 11.37, 22.74, 34.41, 38.97, 45.32, 60.40, and 61.67°2θ for the hydrotalcite phase. The lattice parameters calculated from the peak positions (Table 1) suggested that Gd-incorporated LDH showed no significant differences in unit-cell dimension with respect to the synthesis method. Worth noting, however, is that the peak intensities were modestly different; diffraction peaks of GL-C were quite intense compared with GL-R for all the crystal planes. In order to estimate quantitatively the crystallinity along a certain plane, Scherrer's equation was utilized as follows: $t = (0.9\lambda)/(B \cdot \cos\theta)$ where $t$ = crystallite size, λ = X-ray wavelength, $B$ = full-width-at-half-maximum, θ = Bragg angle. As shown in Table 1, the crystallite size of GL-R was 10.43 and 5.70 nm along the (110) and (003) planes, respectively; on the other hand, the crystallite sizes for GL-C were 12.93 and 14.46 nm for the (110) and (003) planes, respectively. In other words, GL-C had 1.24 times and 2.54 times more ordered arrangements along the (110) and (003) directions, respectively, than GL-R. As expected, the crystal growth of GL-R was restrained, producing thin, platy particles, whereas GL-C was composed mainly of thick particles (Fig. 1).

Taking into account the systemic application of GL-R as a contrasting agent for CT and MRI, the recommendation is that the particle size be controlled at <200 nm to avoid unexpected blood-vessel clogging (Peters et al., 2006; Hoshyar et al., 2016). In this regard, the hydrodynamic radii of GL-R and GL-C were measured by dynamic light scattering (DLS). GL-R showed a single peak at 67.2 nm, while GL-C showed multiple peaks centered at 841.2, 2,163, and beyond 10,000 nm (Fig. 3), meaning that: (1) the primary particle size of GL-C was larger than that of GL-R; and (2) particles of GL-R were dispersed homogeneously while GL-C were assembled to form large agglomerates. The Z-average of GL-R (105.95 ± 3.45 nm) was 20 times smaller than that of GL-C (2097.2 ± 394.70 nm), confirming the large aggregates in GL-C. The degree of homogeneous dispersion was represented quantitatively by the polydispersity index (PDI): 0.70 ± 0.13 and 0.19 ± 0.00 for GL-C and GL-R, respectively. According to the literature, a PDI value of <0.2 means a monodisperse system, while a value of >0.7 means a broad and polydispersive system (Ribeiro et al., 2017; Danaei et al., 2018). The colloidal property of GL-R hybrid was monitored for 7 days. As shown in Fig. S2 and Table S1 (Supplementary Information), colloidal parameters such as Z-average, hydrodynamic radius, PDI value, etc. of GL-R hybrids did not change significantly over 7 days, suggesting that the colloidal stability was good. Thus, a highly monodisperse particle-size distribution of GL-R in aqueous conditions was corroborated by PDI values. As expected from Fig. 1, the reverse micelle system provided a confined space for crystal growth, and interparticle interaction throughout the system was, therefore, fairly restricted. Therefore, GL-R particles had less chance to encounter each other, resulting in the small particles and less agglomeration.

Electron microscopy was used to cross-confirm the particle-size distribution result obtained from DLS. The primary particles of the GL-R were distributed homogeneously without showing significant aggregates (Fig. 4a). The particle size of GL-R was <100 nm as depicted in the Fig. 4a inset image. Although the primary particle of GL-C(Fig. 4b) was <100 nm, most of the particles were assembled together to form clumps which were >5 μm.

Microscopic analyses based on TEM and FFT were carried out to investigate differences between GL-R and GL-C in terms of local crystal structure and morphology. Similar to the results obtained from DLS (Fig. 3) and SEM (Fig. 4), TEM also showed different degrees of dispersion in GL-R and GL-C. While GL-R showed small assemblages consisting of ~30 particles within the range ~100–150 nm (Fig. 5a), GL-C exhibited huge aggregations of >1 μm (Fig. 5d). High-resolution images showed lattice fringes of GL hybrids (Fig. 5b, e), which were attributed to the (015), (018), and (113) lattice planes (Fig. 5c, f). The lattice fringes were aligned in various directions (Fig. 5c,f), suggesting that the primary particles of LDHs were arranged randomly, possibly forming inter-particle cavities.

Several approaches have been attempted to intercalate Gd-DTPA in the interlayer space of LDH to serve as a potential MRI contrasting agent (Xu et al., 2007; Kim et al., 2008; Sun Zhou et al., 2019). Although intercalation of Gd-DTPA is the

https://doi.org/10.1007/s42860-021-00142-9 Published online by Cambridge University Press

best way in terms of stabilization and molecular arrangement, it has several drawbacks. Usually, ion-exchange based intercalation requires a high concentration of guest molecule to achieve a sufficient concentration gradient. Furthermore, the molecular size of Gd-DTPA is larger than the interlayer volume provided by LDH. The molecular volume of Gd-DTPA calculated by its bulk density (1.13 g/cm$^3$) is 800 Å$^3$ with 2(–) charges. On the other hand, the Gd-DTPA-intercalated LDH can give <600 Å$^3$ per 2(+) charges (25 Å$^2$/(+) of unit cell area (Oh et al., 2006a) × 10 Å of interlayer distance (Kim et al., 2008)). The interlayer of LDH, therefore, does not provide sufficient space for Gd-DTPA to be accommodated, resulting in the co-intercalation of small anions such as carbonate and nitrate (Xu et al., 2007; Kim et al., 2008). Unlike previous approaches to intercalation, the current material incorporated Gd-DTPA in the inter-particle space of LDH, resulting in the facilitated accommodation of guest molecules.

This difference was shown by the greater encapsulation efficiency (EE; (Gd-DTPA incorporated into LDH)/(Gd-DTPA utilized in reaction). The chemical formula of GL-R determined by ICP-OES was $Mg_{3.07}Al_1(OH)_8(CO_3^{2-})_{0.37}(Gd\text{-}DTPA)_{0.13}$ showing that Gd-DTPA loading was fairly efficient. The EE and loading capacity (LC) of the current study were 20.8 and 24.7%, respectively, when high Gd amount (Gd/Al =1) was utilized. On the other hand, previous reports on Gd-DTPA intercalation into MgAl-LDH by ion-exchange showed respective EE and LC values of 17.3 and 29.9%, respectively, for a Gd/Al ratio of 1 (Xu et al., 2007); another study on Gd-LDH showed EE and LC values of 33.0 and 33.9% at a Gd/Al ratio of 1.2 (Kim et al., 2008). This means that when the same amount of Gd-DTPA is administered, the amount of Gd moiety which is incorporated into LDH is more efficient in GL-R than elsewhere. The encapsulation strategy of the current research could, therefore, accommodate sufficient Gd-DTPA with a small guest concentration.

The intact structure of Gd-DTPA in GL-R hybrid was identified by FTIR. The IR spectrum of Gd-DTPA showed typical absorption peaks of DTPA chelate at 1320 and 1092 cm$^{-1}$ attributed to $\nu_s$(C-N) and $\nu_s$(C-O), respectively (Ionescu et al., 2017). Only one peak was observed at 1360 cm$^{-1}$ coming from $CO_3^{2-}$ vibrations in the spectrum of MgAl-LDH(Fig. 6c). The representative peaks from both Gd-DPTA(Fig. 6) and MgAl-LDH were also found in the IR spectrum of GL-R. The $\nu_s$(C-N) vibration occurred as a humped peak having a small side shoulder due to the strong absorption of $CO_3^{2-}$. This indicated that the Gd-DTPA moiety was well preserved in the GL-R hybrid. Furthermore, the $\nu_{as}(COO^-)$ and $\nu_{sym}(COO^-)$ of Gd-DTPA were found at 1571 and 1442 cm$^{-1}$; those of GL-R were observed at comparable wavenumber positions. According to previous research, the difference between $\nu_{as}(COO^-)$ and $\nu_{sym}(COO^-)$, i.e. $\Delta\nu$, is related to the coordination mode and geometry of carboxylate (Deacon & Phillips, 1980; Choy et al., 1998; Yang et al., 2007). As the $\Delta\nu$ of Gd-DTPA and GL-R was between 150 and 200 cm$^{-1}$, the DTPA moiety in both samples is expected to be preserved in a unidentate chelating mode.

Because Gd-DTPA was incorporated in LDH under $OH^-$-rich conditions, Gd-DTPA may have hydrolyzed to form an unexpected complex. XPS analysis was, thus, carried out to investigate the chemical properties of Gd-DTPA after incorporation in the GL-R hybrid. The XPS spectrum of GL-R was

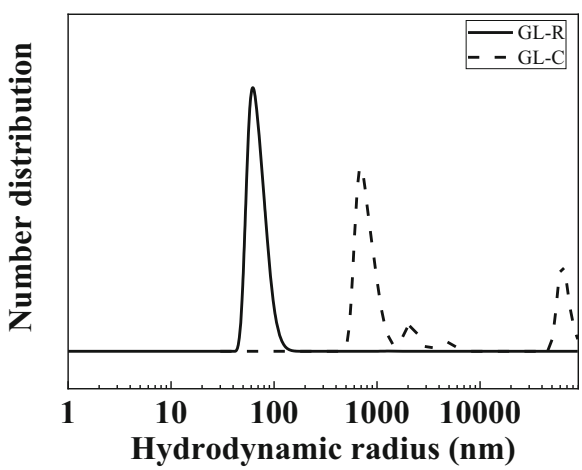



**Fig. 3** Hydrodynamic radii of GL-R and GL-C

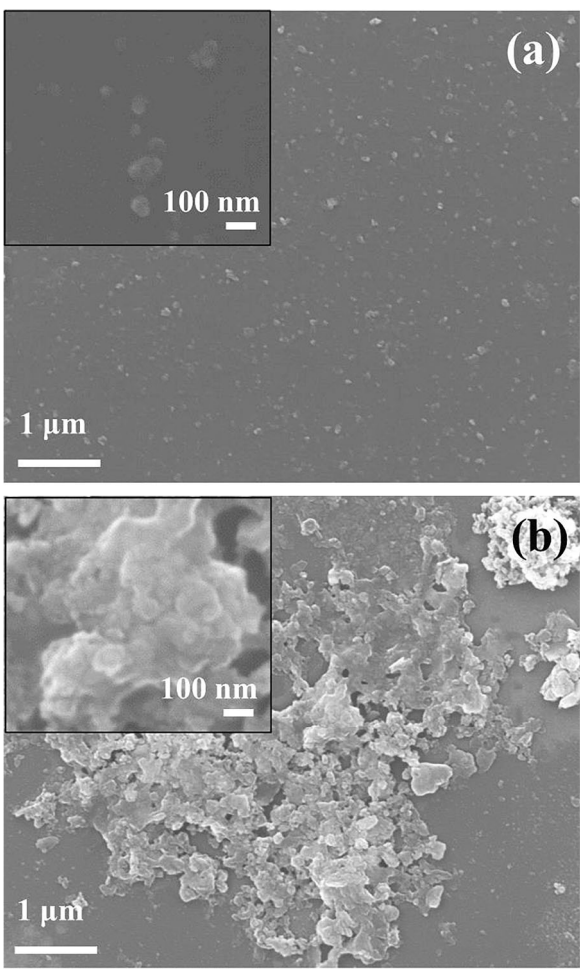



**Fig. 4** SEM images of **a** GL-R and **b** GL-C

https://doi.org/10.1007/s42860-021-00142-9 Published online by Cambridge University Press

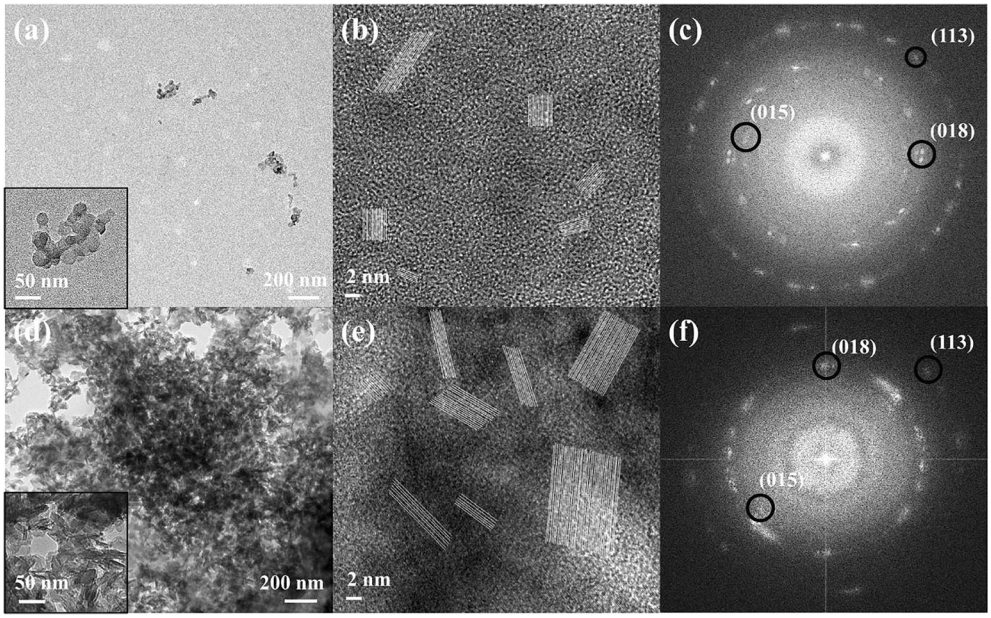



**Fig. 5** **a**, **d** TEM images, **b**, **e**high-resolution images, and **c**, **f** FFT patterns for **a**–**c**GL-R and **d**–**f** GL-C

compared with that of Gd-DPTA with respect to Gd $4d_{5/2}$ and Gd $4d_{3/2}$. The XPS spectrum of Gd-DTPA(Fig. 7a) showed peaks at 146.83 and 141.75 eV for Gd $4d_{3/2}$ and Gd $4d_{5/2}$, respectively (Pan et al., 2017). The XPS profile of GL-R exhibited two peaks for Gd $4d_{3/2}$ and Gd $4d_{5/2}$ which were at binding energies of 146.66 and 141.93 eV, respectively, similar to those for Gd-DTPA. In Fig. 7b, the N 1s electron in GL-R had a binding energy of 398.71 eV, which was similar to the N 1s peak of Gd-DTPA (398.85 eV) attributed to a C–N bond in the DTPA chelate (Fig. 7b) (Zatsepin et al., 2018). The result, in parallel with the FTIR study, suggested that GL-R contained, intact, the structure of Gd-DTPA in the hybrid. One of the possible Gd-complex impurities under the current synthesis conditions is the hydrolysis product, $Gd(OH)_3$. The formation of $Gd(OH)_3$ in the GL-R hybrid was excluded, however, because the Gd $4d_{3/2}$ peak at 147.6 eV, attributed to $Gd(OH)_3$, was absent (Ullah et al., 2017). The small peak at ~152.3 eV was attributed to ligand-to-metal charge transfer (Zatsepin et al., 2018); at this stage, however, why a charge-transfer band developed in GL-R is unclear.

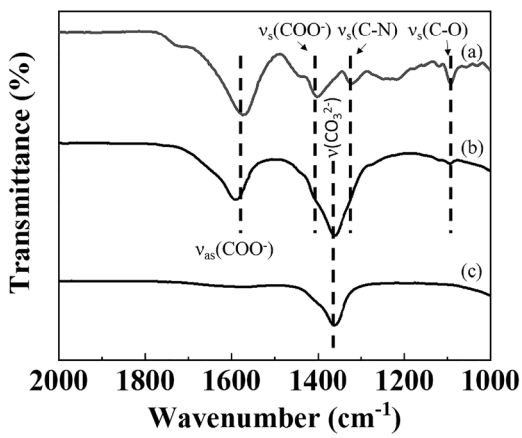



**Fig. 6** FTIR spectra of **a** Gd-DTPA, **b** GL-R, and **c** MgAl-LDH

To check the CT contrasting ability of GL-R, concentration-dependent X-ray attenuation was performed (Fig. 8). In the concentration range of 0.2–2.0 mg/mL, GL-R showed HU values of between 190 and 230. As represented in the inset of Fig. 8, the HU values increased with concentration with a high regression coefficient of 0.9478. Considering that commercial iodinated CT contrast agent, Omnipaque™, shows 140 HU at 10 mg/mL(Li et al., 2019), the current GL-R is considered to have sufficiently high X-ray attenuation of ~190 HU even at the low concentration of 0.2 mg/mL. The HU value of LDH itself showed no significant concentration dependence (Fig. S1) and the values were no different from those of body organs. The Gd-DTPA moiety incorporated in the GL-R hybrid was, therefore, concluded to have played an important role in the CT contrasting property, and the Gd-DTPA was incorporated stably within the inter-particle space made by LDH nanoplates.

The dependence of GL-R as $T_1$-MRI CA on $Gd^{3+}$ concentration was investigated (Fig. 9). As the concentration of the contrast moiety increased, the $1/T_1$ value increased and the brightness of the MR image also increased linearly. Linear regression analysis between $[Gd^{3+}]$ and $1/T_1$ showed high linearity with a regression coefficient of 0.9969. This kind of concentration dependence was expected, as a greater concentration would result in more contact with protons and, thus, enhance the contrast in the image (Caravan et al., 1999; Na et al., 2007). The $T_1$ relaxivity ($r_1$) was measured to check the contrasting ability of GL-R in a $T_1$-weighted image. The $r_1$ value of GL-R was determined to be 5.8, which was comparable with 3.87 of $r_1$ of commercial Gd-DTPA, Magnevist® (Gao et al., 2017).

https://doi.org/10.1007/s42860-021-00142-9 Published online by Cambridge University Press

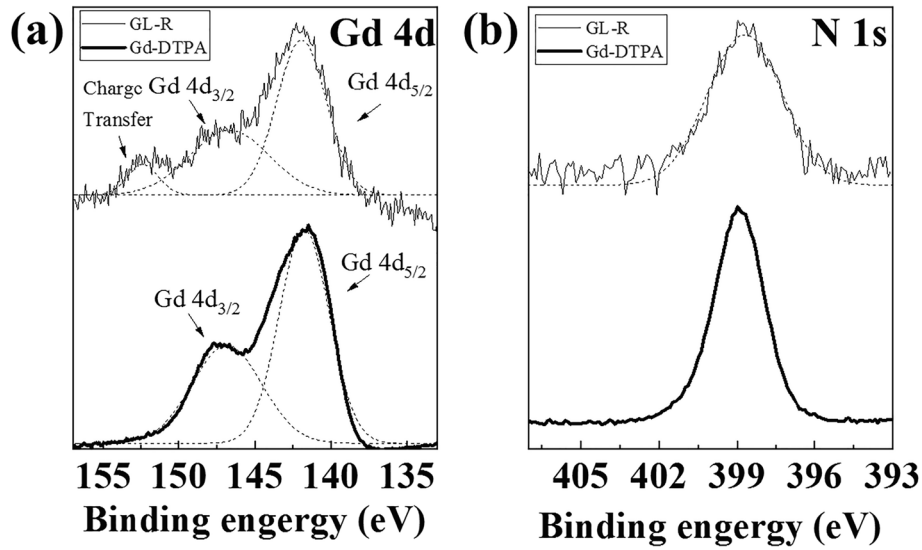



**Fig. 7** XPS spectra of **a** Gd 4d and **b** N 1s for GL-R and Gd-DTPA

## CONCLUSIONS

A gadolinium complex, Gd-DTPA, was incorporated in the assembly of LDH platelets through the reverse-micelle method. Compared with coprecipitation, which usually produces large aggregations/agglomerations, the reverse-micelle method controlled efficiently the particle size of the Gd-DTPA/LDH hybrid, keeping it as small as possible with an homogeneous particle size of 150 nm. The hybrid particle maintained its monodispersity under hydrodynamic conditions, implying its biocompatibility at a systemic level. In TEM and FFT patterns, interparticle cavities were expected, resulting from the randomly arranged LDH nanoplatelets. Spectroscopic analyses, FTIR and XPS, confirmed that the Gd-DTPA moiety preserved its structure intact after incorporation in LDH. Chemical quantification revealed that the encapsulation efficiency of Gd-DTPA in the hybrid was fairly high despite small Gd/Al ratios of reactant. The possibility of the hybrid serving as a CT/MRI dual modal contrasting agent was checked by concentration-dependent HU and $T_1$ measurements, resulting in ~230 HU at 2 mg/mL and 5.8 of $r_1$ relaxivity, respectively; the values were comparable with those of commercial, single-mode contrasting agents.

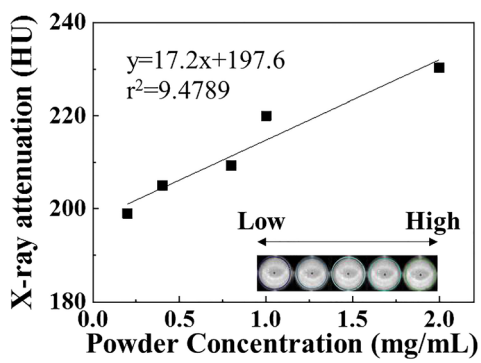



**Fig. 8** CT values of GL-R

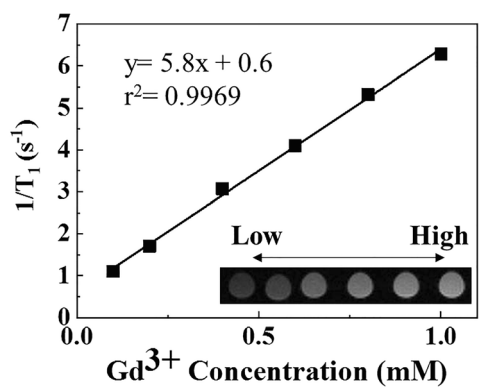



**Fig. 9** $T_1$ relaxivity plot and MR images of GL-R

## ACKNOWLEDGMENT

This research was supported by the Dongguk University Research Fund of 2019.

## FUNDING

Funding sources are as stated in the Acknowledgment.

**Declarations**

**Conflict of Interest**

The authors declare that they have no conflict of interest.

## REFERENCE

Aime, S., & Caravan, P. (2009). Biodistribution of gadolinium-based contrast agents, including gadolinium deposition. *Journal of Magnetic Resonance Imaging, 30*, 1259–1267.

Alauddin, M. M. (2012). Positron emission tomography (PET) imaging with 18F-based radiotracers. *American Journal of Nuclear Medicine and Molecular Imaging, 2*, 55–76.

https://doi.org/10.1007/s42860-021-00142-9 Published online by Cambridge University Press

Bloem, J. L., & Wondergem, J. (1989). Gd-DTPA as a contrast agent in CT. *Radiology, 171*, 578–579.

Caravan, P., Ellison, J. J., McMurry, T. J., & Lauffer, R. B. (1999). Gadolinium(III) chelates as MRI contrast agents: Structure, dynamics, and applications. *Chemical Review, 99*, 2293–2352.

Choi, S. J., Oh, J. M., & Choy, J. H. (2010). Biocompatible nanoparticles intercalated with anticancer drug for target delivery: Pharmacokinetic and biodistribution study. *Journal of Nanoscience and Nanotechnology, 10*, 2913–2916.

Choy, J.-H. (2004). Intercalative route to heterostructured nanohybrid. *Journal of Physics and Chemistry of Solids, 65*, 373–383.

Choy, J.-H., Jung, J.-S., Oh, J.-M., Park, M., Jeong, J., Kang, Y.-K., & Han, O.-J. (2004). Layered double hydroxide as an efficient drug reservoir for folate derivatives. *Biomaterials, 25*, 3059–3064.

Choy, J.-H., Kim, Y.-K., Son, Y.-H., Choy, Y. B., Oh, J.-M., Jung, H., & Hwang, S.-J. (2008). Nanohybrids of edible dyes intercalated in znal layered double hydroxides. *Journal of Physics and Chemistry of Solids, 69*, 1547–1551.

Choy, J.-H., Kwak, S.-Y., Jeong, Y.-J., & Park, J.-S. (2000). Inorganic layered double hydroxides as nonviral vectors. *Angewandte Chemie International Edition, 39*, 4041–4045.

Choy, J.-H., Kwon, Y.-M., Han, K.-S., Song, S.-W., & Chang, S. H. (1998). Intra- and inter-layer structures of layered hydroxy double salts, $Ni_{1-x}Zn_{2x}(OH)_2(CH_3CO_2)_{2x}{\cdot}nH_2O$. *Materials Letters, 34*, 356–363.

Danaei, M., Dehghankhold, M., Ataei, S., Hasanzadeh Davarani, F., Javanmard, R., Dokhani, A., Khorasani, S., & Mozafari, M. R. (2018). Impact of particle size and polydispersity index on the clinical applications of lipidic nanocarrier systems. *Pharmaceutics, 10*, 57.

Deacon, G. B., & Phillips, R. J. (1980). Relationships between the carbon-oxygen stretching frequencies of carboxylato complexes and the type of carboxylate coordination. *Coordination Chemistry Reviews, 33*, 227–250.

Gao, L., Zhou, J., Yu, J., Li, Q., Liu, X., Sun, L., et al. (2017). A novel Gd-DTPA-conjugated poly(l-γ-glutamyl-glutamine)-paclitaxel polymeric delivery system for tumor theranostics. *Scientific Reports,7,* 3799.

Gursky, J. A., Blough, S. D., Luna, C., Gomez, C., Luevano, A. N., & Gardner, E. A. (2006). Particle–particle interactions between layered double hydroxide nanoparticles. *Journal of the American Chemical Society, 128*, 8376–8377.

Hoshyar, N., Gray, S., Han, H., & Bao, G. (2016). The effect of nanoparticle size on in vivo pharmacokinetics and cellular interaction. *Nanomedicine (Lond), 11*, 673–692.

Hu, G., Wang, N., O'Hare, D., & Davis, J. (2007). Synthesis of magnesium aluminium layered double hydroxides in reverse microemulsions. *Journal of Materials Chemistry, 17*, 2257–2266.

Ionescu, E., Li, W., Wiehl, L., Mera, G., & Riedel, R. (2017). Synthesis of nanocrystalline $Gd_2O_2NCN$ from a versatile single-source precursor. *Zeitschrift für anorganische und allgemeine Chemie, 643*, 1681–1691.

Kim, H. J., Ryu, K., Kang, J. H., Choi, A. J., Kim, T. I., & Oh, J. M. (2013). Anticancer activity of ferulic acid-inorganic nanohybrids synthesized via two different hybridization routes, reconstruction and exfoliation-reassembly. *Scientific World Journal, 2013*, 421967.

Kim, S. Y., Oh, J. M., Lee, J. S., Kim, T. J., & Choy, J. H. (2008). Gadolinium (III) diethylenetriamine pentaacetic acid/ layered double hydroxide nanohybrid as novel T1-magnetic resonant nanoparticles. *Journal of Nanoscience and Nanotechnology, 8*, 5181–5184.

Kim, T.-H., Kim, H., & Oh, J.-M. (2012). Interlayer structure of bioactive molecule, 2-aminoethanesulfonate, intercalated into calcium-containing layered double hydroxides. *Journal of Nanoscience and Nanotechnology, 2012, article 21*. https://doi.org/10.1155/2012/987938

Kim, T.-H., Lee, G. J., Kang, J.-H., Kim, H.-J., Kim, T.-I., & Oh, J.-M. (2014). Anticancer drug-incorporated layered double hydroxide nanohybrids and their enhanced anticancer therapeutic efficacy in combination cancer treatment. *BioMed Research International, 2014*, 193401.

Kim, T.-H., Lee, J. Y., Kim, M.-K., Park, J. H., & Oh, J.-M. (2016). Radioisotope Co-57 incorporated layered double hydroxide nanoparticles as a cancer imaging agent. *RSC Advances, 6*, 48415–48419.

Kriven, W. M., Kwak, S.-Y., Wallig, M. A., & Choy, J.-H. (2004). Bio-resorbable nanoceramics for gene and drug delivery. *MRS Bulletin, 29*, 33–37.

Li, L., Jiang, W., Luo, K., Song, H., Lan, F., Wu, Y., & Gu, Z. (2013a). Superparamagnetic iron oxide nanoparticles as mri contrast agents for non-invasive stem cell labeling and tracking. *Theranostics, 3*, 595–615.

Li, Z., Wang, S. X., Sun, Q., Zhao, H. L., Lei, H., Lan, M. B., Cheng, Z. X., Wang, X. L., Dou, S. X., & Lu, G. Q. (2013b). Ultrasmall manganese ferrite nanoparticles as positive contrast agent for magnetic resonance imaging. *Advanced Healthcare Materials, 2*, 958–964.

Li, B., Gu, Z., Kurniawan, N., Chen, W., & Xu, Z. P. (2017). Manganese-based layered double hydroxide nanoparticles as a T(1) -mri contrast agent with ultrasensitive pH response and high relaxivity. *Advanced Materials, 29*, 1700373.

Li, X., Liu, Y., Fu, F., Cheng, M., Liu, Y., Yu, L., Wang, W., Wan, Y., & Yuan, Z. (2019). Single nir laser-activated multifunctional nanoparticles for cascaded photothermal and oxygen-independent photodynamic therapy. *Nano-Micro Letters, 11*, 68.

Lusic, H., & Grinstaff, M. W. (2013). X-ray-computed tomography contrast agents. *Chemical Reviews, 113*, 1641–1666.

Ma, S., & Liu, Y. (2020). Diagnostic value of fluorine-18 fluorodeoxyglucose positron emission tomography/computed tomography in sublingual and submandibular salivary gland tumors. *Molecular and Clinical Oncology, 13*, 27.

Meng, D., Cui, X., Bai, C., Yu, Z., Xin, L., Fu, Y., Wang, S., Du, Y., Gao, Z., & Ye, Z. (2019). Application of low-concentration contrast agents and low-tube-voltage computed tomography to chest enhancement examinations: A multicenter prospective study. *Science Progress, 103*, 0036850419892193.

Musumeci, A., Schiller, T., Xu, Z., Minchin, R., Martin, D., & Smith, S. (2010). Synthesis and characterization of dual radiolabeled layered double hydroxide nanoparticles for use in in vitro and in vivo nanotoxicology studies. *The Journal of Physical Chemistry C, 114*(2), 734–740.

Na, H., Jung, L., An, K., Park, Y. I., Park, M., Lee, I., Nam, D.-H., Kim, S. T., Kim, S.-H., Kim, S.-W., Lim, K.-H., Kim, K., Kim, S.-O., & Hyeon, T. (2007). Development of at1 contrast agent for magnetic resonance imaging using mno nanoparticles. *Angewandte Chemie (International ed. in English), 46*, 5397–5401.

Oh, J.-M., Kwak, S.-Y., & Choy, J.-H. (2006a). Intracrystalline structure of DNA molecules stabilized in the layered double hydroxide. *Journal of Physics and Chemistry of Solids, 67*, 1028–1031.

Oh, J.-M., Park, M., Kim, S.-T., Jung, J.-Y., Kang, Y.-G., & Choy, J.-H. (2006b). Efficient delivery of anticancer drug MTX through MTX-LDH nanohybrid system. *Journal of Physics and Chemistry of Solids, 67*, 1024–1027.

Oh, J. M., Choi, S. J., Lee, G. E., Kim, J. E., & Choy, J. H. (2009). Inorganic metal hydroxide nanoparticles for targeted cellular uptake through clathrin-mediated endocytosis. *Chemistry: An Asian Journal, 4*, 67–73.

Pan, Y., Yang, J., Fang, Y., Zheng, J., Song, R., & Yi, C. (2017). One-pot synthesis of gadolinium-doped carbon quantum dots for high-performance multimodal bioimaging. *Journal of Materials Chemistry B, 5*, 92–101.

Pedrosa, P., & Baptista, P. V. (2015). Chapter 1 - gold and silver nanoparticles for diagnostics of infection. In M. Rai & K. Kon (Eds.), *Nanotechnology in diagnosis, treatment and prophylaxis of infectious diseases* (pp. 1–18). Academic Press.

Peters, A., Veronesi, B., Calderón-Garcidueñas, L., Gehr, P., Chen, L. C., Geiser, M., Reed, W., Rothen-Rutishauser, B., Schürch, S., &

https://doi.org/10.1007/s42860-021-00142-9 Published online by Cambridge University Press

Schulz, H. (2006). Translocation and potential neurological effects of fine and ultrafine particles a critical update. *Particle and Fibre Toxicology, 3*, 13.

Ribeiro, L. N. M., Breitkreitz, M. C., Guilherme, V. A., da Silva, G. H. R., Couto, V. M., Castro, S. R., de Paula, B. O., Machado, D., & de Paula, E. (2017). Natural lipids-based nlc containing lidocaine: From pre-formulation to in vivo studies. *European Journal of Pharmaceutical Sciences, 106*, 102–112.

Seltzer, S. E., Shulkin, P. M., Adams, D. F., Davis, M. A., Hoey, G. B., Hopkins, R. M., & Bosworth, M. E. (1984). Usefulness of liposomes carrying losefamate for CT opacification of liver and spleen. *American Journal of Roentgenology, 143*, 575–579.

Sun Zhou, X.D., Marzke, R., Peng, Z., Szilágyi, I., & Dey, S.K. (2019). Understanding the high longitudinal relaxivity of Gd(DPTA)-intercalated (Zn,Al)-layered double hydroxide nanoparticles. *Inorganic Chemistry*, *58*, 12112–12121.

Ullah, N., Imran, M., Liang, K., Yuan, C.-Z., Zeb, A., Jiang, N., Qazi, U., Sahar, S., & Xu, A.-W. (2017). Highly dispersed ultra-small pd nanoparticles on gadolinium hydroxide nanorods for efficient hydrogenation reactions. *Nanoscale, 9*, 13800–13807.

Vithanarachchi, S. M., & Allen, M. J. (2012). Strategies for target-specific contrast agents for magnetic resonance imaging. *Current molecular imaging, 1*, 12–25.

Wattjes, M. P., Steenwijk, M. D., & Stangel, M. (2015). Mri in the diagnosis and monitoring of multiple sclerosis: An update. *Clinical Neuroradiology, 25*, 157–165.

Xie, W., Guo, Z., Cao, Z., Gao, Q., Wang, D., Boyer, C., Kavallaris, M., Sun, X., Wang, X., Zhao, L., & Gu, Z. (2019). Manganese-based magnetic layered double hydroxide nanoparticle: A pH-sensitive and concurrently enhanced T1/T2-weighteddual-mode magnetic resonance imaging contrast agent. *ACS Biomaterials Science & Engineering, 5*, 2555–2562.

Xu, C., Akakuru, O. U., Zheng, J., & Wu, A. (2019). Applications of iron oxide-based magnetic nanoparticles in the diagnosis and treatment of bacterial infections. *Frontiers in Bioengineering and Biotechnology, 7*, 141–141.

Xu, Z. P., Kurniawan, N. D., Bartlett, P. F., & Lu, G. Q. (2007). Enhancement of relaxivity rates of Gd-dtpa complexes by intercalation into layered double hydroxide nanoparticles. *Chemistry – A European Journal, 13*, 2824–2830.

Yang, J.-H., Han, Y.-S., Park, M., Park, T., Hwang, S.-J., & Choy, J.-H. (2007). New inorganic-based drug delivery system of indole-3-aceticacid-layered metal hydroxide nanohybrids with controlled release rate. *Chemistry of Materials, 19*, 2679–2685.

Zatsepin, D. A., Boukhvalov, D. W., Zatsepin, A. F., Kuznetsova, Y. A., Mashkovtsev, M. A., Rychkov, V. N., Shur, V. Y., Esin, A. A., & Kurmaev, E. Z. (2018). Electronic structure, charge transfer, and intrinsic luminescence of gadolinium oxide nanoparticles: Experiment and theory. *Applied Surface Science, 436*, 697–707.

Zhang, J., Ju, X., Wu, Z. Y., Liu, T., Hu, T. D., Xie, Y. N., & Zhang, Z. L. (2001). Structural characteristics of cerium oxide nanocrystals prepared by the microemulsion method. *Chemistry of Materials, 13*, 4192–4197.

Zhang, Y., Li, B., Wu, B., Yu, H., Song, J., Xiu, Y., & Shi, H. (2020). Diagnostic performance of whole-body bone scintigraphy in combination with spect/ct for detection of bone metastases. *Annals of Nuclear Medicine, 34*, 549–558.

(*Received 23 March 2021; revised 14 July 2021; AE: Yuji Arai*)

https://doi.org/10.1007/s42860-021-00142-9 Published online by Cambridge University Press